Application of smoothed particle hydrodynamics (SPH) and pore morphologic model 2 to predict saturated water conductivity from X-ray CT imaging in a silty loam Cambisol

N. Dal Ferro, A.G. Strozzi,, Céline Duwig, P. Delmas, P. Charrier, F. Morari,

Geoderma xxx (2015) xxx–xxx

Contents lists available at ScienceDirect

Geoderma

journal homepage: www.elsevier.com/locate/geoderma

Application of smoothed particle hydrodynamics (SPH) and pore morphologic model to predict saturated water conductivity from X-ray CT imaging in a silty loam Cambisol

N. Dal Ferro [a,*], A.G. Strozzi [b], C. Duwig [c], P. Delmas [d], P. Charrier [e], F. Morari [a]

[a] Department of Agronomy, Food, Natural resources, Animals and Environment, Agripolis, University of Padova, Viale Dell'Università 16, 35020 Legnaro, Padova, Italy
[b] UNAM, CCADET, Ciudad Universitaria, Mexico Cuidad, Mexico
[c] IRD/UJF-Grenoble 1/CNRS/G-INP, LTHE, UMR 5564, BP 53, 38041 Grenoble Cedex 9, France
[d] Department of Computer Science, The University of Auckland, Private Bag 92019, New Zealand
[e] Laboratoire 3S-R, CNRS/UMR/UJF/INP BP 53, 38041 Grenoble Cedex 9, France

ARTICLE INFO

Article history:
Received 24 January 2015
Received in revised form 1 April 2015
Accepted 16 April 2015
Available online xxxx

Keywords:
X-ray computed microtomography
Saturated hydraulic conductivity
Soil structure
Pore size distribution

ABSTRACT

This study aims to estimate saturated hydraulic conductivity in a silty loam soil and compare modelled data with experimental ones. The flow characteristics of twelve undisturbed soil cores (5 cm in diameter × 6 cm high) were measured in the laboratory after performing X-ray computed microtomography (microCT) analysis. MicroCT 3D imaging was integrated with an existing pore morphologic model and a numerical simulation based on mesh-free smoothed particle hydrodynamics (SPH) to calculate the water flow through the macropore network (pores > 40 μm). Results showed that the proposed SPH method was able to predict hydraulic conductivity of large-sized samples as falling in the range of the experimental ones. By contrast the morphologic model generally underestimated the water flow and was slightly affected by the pore shape. Increasing microCT imaging resolution and expanding the variability with other soil types will improve the understanding of the role of micropore size and morphology on water conductivity.

1. Introduction

Reliable estimation of fluid flow and transport through porous media is crucial for several disciplines including geosciences and water resources management. Great efforts focused on indirect methods for water flow predictions in porous media which mainly considered the physical media characteristics (specific surface, grain and pore size etc.) (Arya et al., 2010; Kozeny, 1953). However, these methods are suitable for homogeneous and simplified pore networks with little or no organic matter (Chapuis, 2012). Some explicit approaches referring to natural soils are mostly based on regression equations as the pedotransfer functions (PTFs) (Bouma, 1989). Despite the extensive literature (e.g., Pachepsky et al., 2006; Vereecken et al., 2010) and large databases on soil characteristics as a result of PTFs (Leij et al., 1996; Lilly, 1996), the accuracy and reliability of PTFs may be appropriate on regional or national scale, whereas they are not recommended at specific points (plot or microscopic scales) and when soils are outside the type of those used to derive the PTFs (Wösten et al., 2001). Experimental application of Darcy's law is the main direct method to measure the laminar water flow both in laboratory and in the field, which was directly correlated to micro-scale governing equations based on Stokes' law (Bear, 1972). Since recent advances on experimental analysis and image processing techniques through X-ray computed microtomography (microCT), which allows the reconstruction of real structure properties, pore level models have been developed with the aim to solve partial differential equations using numerical techniques. The great advantage of having inside images of the undisturbed soil pore network is to overtake the concept of the capillary bundle model while studying the soil in its three-dimensional space (Hunt et al., 2013).

Remarkable results were shown by Narsilio et al. (2009) who estimated saturated hydraulic conductivity on uniform granular material. Following the derivation introduced by Bear and Bachmat (1990) that links the macroscopic phenomenological Darcy's law and the pore-scale Stokes' equations, the authors estimated successfully the water flow by solving directly the Navier–Stokes equation at the pore scale. However the structural complexity of much more reliable natural soils is very difficult to model as a consequence of high demand of computational work. Moreover, the generation of a quality mesh, prerequisite for accurate numerical simulations, has become time inefficient and expensive.

Alternative approaches, such as Lagrangian particle-based methods, have been proposed with the aim to handle computational load more easily and speed up computer simulations. Lattice-Boltzmann, diffuse element method (DEM) and smoothed particle hydrodynamics (SPH) are mesh-free computer simulation techniques, easy to design and suitable for random and deformable porous media (Liu and Liu, 2003). SPH

* Corresponding author.
E-mail address: nicola.dalferro@unipd.it (N. Dal Ferro).

http://dx.doi.org/10.1016/j.geoderma.2015.04.019
0016-7061/

is promising for direct simulation of multi-phase material behaviour at multiple scale (Liu and Liu, 2010). As such it is particularly well adapted to simulating flow and flow-solid multi-scale interaction in real porous structure by linking observed soil structure and its transport function. Due to its molecular structure, SPH modelling can make the best out of parallel implementation on GPGPU (general purpose graphic processing units). Known weaknesses of SPH modelling are the complexity of interaction at multi-phase interfaces. Despite the growing interest on mesh free methods, only a few have combined this computational approach to soil science in order to quantify physical characteristics on large and complex samples. Ovaysi and Piri (2010) developed a moving particle semi-implicit method (MPS) and modelled the permeability of a reservoir sandstone previously analysed with X-rays. The authors successfully predicted the intrinsic permeability and validated their model against experimental data. However the representative elementary volume was reduced to *ca.* 1 mm^3 as a result of the uniform pore and throat size (mostly 20–30 μm) in sandstone. Tartakovsky and Meakin (2005), using a numerical model based on smoothed particle hydrodynamic, focused on the three-dimensional fluid flow prediction on fractures generated by self-affine fractal surfaces. They stated that the mesh-free approach was suitable for simulating the surface flow of both wetting and non-wetting fluids in complex fractures, although they also highlighted the need of comparison with laboratory measurements and the application of their model to soil samples that should include a wider pore size distribution. In fact, the assumptions of homogeneity of hydraulic properties are often not met in natural intact samples due to high variability of structure properties. In order to avoid computational complexity in calculating saturated permeability (K_S) of soil cores, Elliot et al. (2010) used 3D pore characteristics derived from X-ray microCT in modified pore fluid transport models (e.g. Darcy's law and Poiseuille's equation), demonstrating the advanced potentialities of the 3D approach.

Our hypothesis is that X-ray microCT can be used to calculate saturated conductivity on large complex soil structures by coupling the quantification of pore network properties and modelling. As a result in this work we compared two different approaches to simulate saturated conductivity using 3D-derived pore information, one based on an innovative numerical model based on smoothed particle hydrodynamic (SPH) and the other based on Darcy's law and modified Poiseuille's equation according to Elliot et al. (2010).

2. Materials and methods

2.1. Soil sampling

The soil samples come from a long-term experiment established in 1962 at the experimental farm of the University of Padova (Italy). The soil is a silty loam Fluvi-Calcaric Cambisol (CMcf) (FAO-UNESCO, 1990). This work considered four treatments characterized by different fertilizations: organic, mineral and no fertilization. Organic fertilizations were farmyard manure (FMY; 60 t ha^{-1} y^{-1}, 20% d.m.) and liquid manure (L; 120 t ha^{-1} y^{-1}, 10% d.m.); mineral input (NPK) was 300 kg N ha^{-1} y^{-1}, 66 kg P ha^{-1} y^{-1}, 348 kg K ha^{-1} y^{-1} while no fertilization control had no inputs (O). Liquid manure input also includes crop residue incorporation (r = 3.7 t C ha^{-1} y^{-1} on average). The same type of soil tillage has been used in all treatments, with autumn ploughing and subsequent cultivations before sowing the main crop. The experimental layout is a randomized block with three replicates, on plots of 7.8 × 6 m. Further details on experimental design are extensively reported in the literature (e.g., Morari et al., 2006). Twelve (4 treatments × 3 replicates, hereafter indicated with subscripts 1, 2, 3) undisturbed soil cores (5 cm diameter, 6 cm length) were collected in August 2010, at the end of the maize season, from the topsoil (5 to 20 cm depth) in polymethylmethacrylate (PMMA) cylinders using a manual hydraulic core sampler (Eijkelkamp, The Netherlands). Successively soil cores were stored at 5 °C before analysis.

2.2. X-ray microtomography and digital image processing and analysis

Soil core scanning was completed at the "3S-R" laboratory in Grenoble (http://www.3sr-grenoble.fr). The X-ray generator was a multi-energy and different spot size (Hamamatsu), with a voltage range of 40–150 kV and intensity of 0–500 μA. The beam open angle was 43°. The detector had the dimension of 1920 × 1536 pixels. All samples were scanned with the same technical parameters that were calibrated as a function of sample dimension, composition and distance from the X-ray beam generator. Setting parameters were 100 kV, 300 μA and projections were collected during a 360° sample rotation at 0.3° angular incremental step. Each angular projection was calculated as the mean of 10 repeated acquisitions. The scan frequency was 7 images s^{-1}. Projections were reconstructed using the dedicated software DigiCT 1.1 (Digisens, France) to obtain a stack of about 1500 2D slices in 32-bit depth. 32-bit images were later converted into 8-bit depth. Final voxel resolution was 40 μm in all three directions.

The digital image processing and analysis were conducted with the public domain image processing ImageJ (Vs. 1.45, National Institute of Health, http://rsb.info.nih.gov/ij). In order to exclude the PMMA sample holder and artefacts caused by edge effects, a cylindrical 3D image dataset, almost equal to the entire soil column, was selected for analysis. The volume had a diameter of 1150 pixels (the original soil cores were 1250 pixels in diameter) and was composed of 1200 slices.

Slices were segmented using a global-threshold value based on the histogram greyscale that was determined by the maximum entropy threshold algorithm. The threshold value was selected where the inter-class entropy was maximized (Luo et al., 2010). Using 8-connectivity, a mathematical morphology closing operator (Serra, 1982) of half-width of 1 was applied to the binary images to fill misclassified pixels inside the pores as well as to maintain pore connections. The structure characterization of 3D stacks included the estimation of total porosity, pore size distribution, tortuosity (τ) and discrete compactness (C_d). BoneJ plugin (Doube et al., 2010), freely available for ImageJ, was used to reconstruct a 3D pore skeleton (Lee et al., 1994) for each sample to determine pore tortuosity as the ratio between the actual pore length and the Euclidean distance along the skeleton. The discrete compactness is a 3D shape factor defined on a scale of 1 (circular or spherical) to 0 (linear or disperse structure) which provides information on the morphology of basic shapes that have been used to represent structures in 3D CT imagery. It was introduced to estimate the pore hydraulic radius as per Bribiesca et al. (2003):

$$C_d = \frac{A_C - A_{Cmin}}{A_{Cmax} - A_{Cmin}}, \quad (1)$$

where A_C is the contact surface area, A_{Cmin} is the minimum contact surface area and A_{Cmax} is the maximum contact surface area (Bribiesca, 2000).

3D pore size distribution was calculated using CTAn software v. 1.12.0.0 (Bruker micro-CT, Kontich, Belgium) from each binarized stack, drawing a sphere inside the 3D pore space that touched the bordering soil matrix and measuring the sphere diameter. The method first identifies the medial axes of all structures and then the sphere-fitting is done for all the voxels lying along this axis (Remy and Thiel, 2002).

2.3. Experimental saturated conductivity (K_S) estimate

After microCT scanning, soil samples were gradually saturated from the bottom up over a 5-day period using temperature-equilibrated tap water. Saturated hydraulic conductivity (K_S, m s^{-1}) was measured using the constant head or falling head method, depending on the soil characteristics and range of K_S that can be measured (Reynolds et al., 2002).

Please cite this article as: Dal Ferro, N., et al., Application of smoothed particle hydrodynamics (SPH) and pore morphologic model to predict saturated water conductivity from X-ray..., Geoderma (2015), http://dx.doi.org/10.1016/j.geoderma.2015.04.019

2.4. Water retention curve estimate

After K_S measurements, the cores were subjected to water retention curve estimate using the Ku-pF apparatus (UGT GmbH, Müncheberg, Germany). Briefly, after saturation two tensiometers were installed at depths of −1.5 cm and −4.5 cm, respectively, from the sample surface. The samples were sealed at the bottom and placed in the apparatus for the combined measurement of sample mass and matric potentials, from which the water retention curves were estimated. Finally, experimental data were interpolated according to the Van Genuchten model (Van Genuchten et al., 1991) using RETC version 6.02. The water retention curves (WRCs) were then used to determine the pore size distribution (PSD) according to the capillary model and the equivalent pore radii were calculated from the matric head by applying the Young–Laplace equation:

$$r = \frac{2\gamma\cos\theta}{P}, \tag{2}$$

where r is the pore radius, P is the matric head, γ is the surface tension of water at 20 °C (0.7286 N m^{-1}) and θ is the contact angle between water and soil (here it was considered to be 0°). Total pore volume was also measured with the gravimetric method as a result of soil cores weighing at saturation and after oven-drying for 24 h at 105 °C.

2.5. Smoothed particle hydrodynamic (SPH) model description and simulations

Smoothed Particle Hydrodynamics (SPH) considers a multi-phase object as a set of particles each representing a discrete volume fraction of the studied object. Each particle has its own mechanical properties summarizing its individual behaviour as governed by the laws of hydrodynamics (Monaghan, 1992).

The physical properties (mass, velocity, energy) of a SPH particle at a given location are approximated by a generic quantity A. A is computed by taking into account the set of discrete particles i, with $i = 1,\ldots,N$, constituting the SPH volume. The value of $A(i)$ for any given particle i depends on all the neighbourhood particles j, the group of which is formed from all the particles constituting the SPH volume, excluding the particle i within a distance h from the particle centred in r_i:

$$A(i) = \sum_{j\neq i} A(j) W\left(r_i - r_j, h\right), \tag{3}$$

where $W(r_i - r_j, h)$ is a smoothing kernel function value at distance $r_i - r_j$. W controls how the particle j inside the smoothing distance h influences the particle i. This function is solved for all the particle i defining the fluid volume. Classically W is often chosen as a cubic spline or Gaussian curve. To simulate the velocity q of fluid particles, incompressible fluid movement was described using a simplified Navier–Stokes equation and interactions between particles were expressed with Hooke's law (Strozzi et al., 2009):

$$\rho\left(\frac{\partial v}{\partial t} + v\cdot\nabla v\right) = -\nabla p + \rho g + \mu\nabla^2 v, \tag{4}$$

where ρ is the fluid density, v is the flow velocity, p is the pressure, μ is the dynamic viscosity and g the gravity at sea-level. The numerical solution of Navier–Stokes equations with the SPH method was implemented as in Liu and Liu (2003).

2.5.1. SPH numerical simulation, initial and limit conditions

Due to given memory requirements, one voxel contains one particle as a sphere. The number of particles within each simulated pores varied depending on its volume. The volume of interaction for each particle with its neighbours was set as a cube of $5 \times 5 \times 5$ voxels for a calculated radius r_i equal to 100 μm. The mass m_i of the particle is the equivalent mass of spherical particle of radius = 20 μm (0.5 voxels) and equals to $3.2 \cdot 10^{-9}$ g. The dynamic viscosity μ was set at 0.001 Pa s. For each pore, the inlet and outlet were chosen as cross-sections (planes perpendicular) to the pore skeleton upper and lower extremities. The initial condition for the flow simulation considers the pores filled with water and assigned the inlet and outlet cross-sections to the voxels belonging to the top and bottom skeleton cross-sections. The pressure difference ΔP between the plane inlet and the outlet was set at 1 Pa which ensures that the Reynolds number is equal or lower than 10, and thus is comfortably in the laminar regime (Narsilio et al., 2009). Once SPH flow simulation in the pores reached permanent state, the flow was computed by summing (integrating) the velocities of all pores across the outlet cross sections. The saturated hydraulic conductivity K_{SPH} was obtained through the Darcy's equation:

$$K = \frac{QL}{A\Delta P}, \tag{5}$$

where Q is the flow through the pores, A is the cross-sectional area of the sample, L is the sample length and ΔP is the change in hydrostatic pressure. K_{SPH} was calculated for the pores representing the highly networked massive singular pore through the entire soil cores (Fig. 1; Table 1).

2.6. K estimate from pore morphologic characteristics

Saturated hydraulic conductivity of the largest pore (K_{MORPHO}) within each stack, representing the highly networked massive singular pore within the soil cores (Dal Ferro et al., 2013), was calculated following the morphologic approach proposed by Elliot et al. (2010). The novelty of the model consisted in combining three dimensional pore shape aspects (i.e. tortuosity and discrete compactness) with the pore volume and using that information in Darcy's equation (Eq. (5)) and a modified Poiseuille equation.

The water flow through the pores (Q) was estimated with a modified Poiseuille equation (Elliot et al., 2010) as follows:

$$Q = \frac{\pi R^4 \Delta P}{8 L_c \nu}, \tag{6}$$

where R is the pore radius, ν is the viscosity of water at room temperature and L_c is the complete pore length. R and L_c were estimated adopting the approach of Elliot et al. (2010) in order to incorporate the pore characteristics in the established model as follows:

$$R = \left(\frac{V}{\pi L_c^{\,c}}\right)^{1/2}, \tag{7}$$

where V is the pore volume and

$$L_c = [(1 - C_d)\tau L], \tag{8}$$

where L is the length of soil core, C_d is the discrete compactness of pore and τ is the tortuosity (see Section 2.2).

2.7. Water conductivity estimate based on the Kozeny–Carman equation

Experimental and modelled water conductivity data were compared with those from a semi-empirical modified Kozeny–Carman equation (Rawls et al., 1998), which uses soil porosity and pore size distribution data to estimate the saturated hydraulic conductivity (K_{KC}) as follows:

$$K_{KC} = C\phi_e^{3-\lambda} \tag{9}$$

Please cite this article as: Dal Ferro, N., et al., Application of smoothed particle hydrodynamics (SPH) and pore morphologic model to predict saturated water conductivity from X-ray..., Geoderma (2015), http://dx.doi.org/10.1016/j.geoderma.2015.04.019

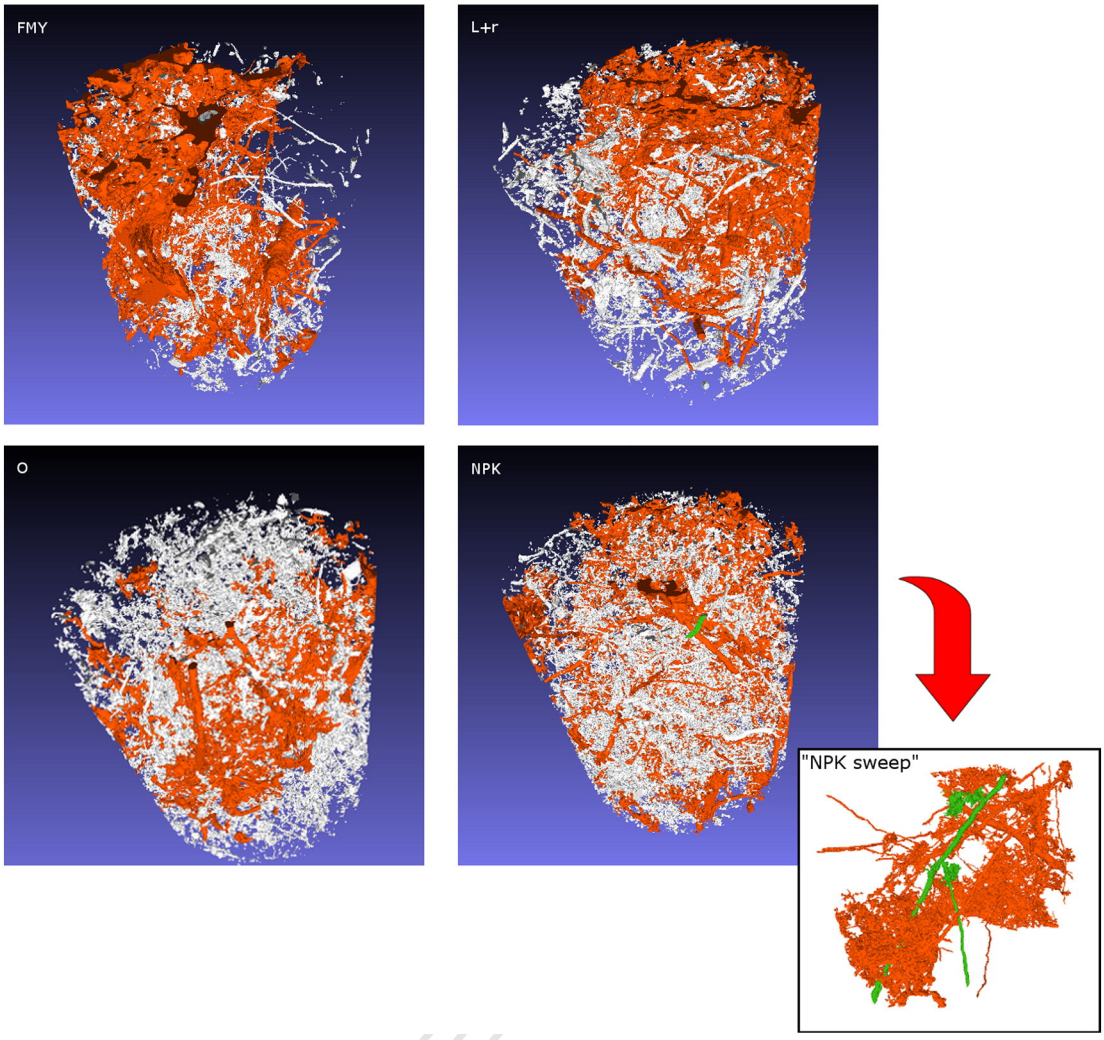

Fig. 1. 3D images of soil pore characteristics (FMY = farmyard manure; L + r = liquid manure + residues; NPK = mineral fertilization; O = no fertilization control) as a result of X-ray microCT. Soil porosity is represented in grey and orange, where the orange pore network represents the highly interconnected pore space and the grey ones represent the remaining porosity. As an example, the NPK sample was wiped from the grey pores ("NPK sweep"), apart from a minor pore (labelled in green) that highlights a secondary water flow through the entire soil core. (For interpretation of the references to color in this figure legend, the reader is referred to the web version of this article.)

where ϕ_e is the effective porosity (total porosity minus water content at −33 kPa; $m^3\ m^{-3}$), C is an empirically derived constant ($5.36 \cdot 10^{-4}$ m s^{-1}, Rawls et al., 1998) and λ is the Brook and Corey pore size distribution index, corresponding to the Van Genuchten pore size distribution parameter n minus 1 (Maidment, 1993).

Table 1
Structure properties of soil cores.

Sample ID	Texture parameters			WRC parameters[a]				MicroCT parameters			
	Sand (%)	Silt (%)	Clay (%)	θ_r	θ_s	α	n	Total porosity ($m^3\ m^{-3}$)	Largest pore ($m^3\ m^{-3}$)	C_d[b]	τ[c]
FMY_1	41.9	54.1	4.0	0.180	0.490	0.031	1.210	0.058	0.053	0.91	4.72
FMY_2	30.4	64.6	4.9	0.000	0.461	0.024	1.168	0.117	0.104	0.85	4.36
FMY_3	30.5	64.3	5.1	0.172	0.476	0.062	1.198	0.045	0.031	0.88	6.35
$L + r_1$	35.5	59.8	4.6	0.000	0.532	0.025	1.173	0.170	0.163	0.96	4.47
$L + r_2$	39.2	56.6	4.2	0.000	0.515	0.148	1.096	0.063	0.052	0.86	5.51
$L + r_3$	34.7	61.1	4.1	0.000	0.481	0.016	1.138	0.015	0.008	0.95	3.75
NPK_1	31.8	62.3	5.9	0.136	0.500	0.056	1.191	0.078	0.068	0.87	5.20
NPK_2	28.1	66.6	5.3	0.000	0.492	0.060	1.106	0.058	0.045	0.84	5.30
NPK_3	32.8	61.8	5.4	0.000	0.521	0.097	1.091	0.051	0.036	0.87	4.37
O_1	25.0	69.6	5.4	0.000	0.459	0.056	1.058	0.037	0.020	0.84	6.58
O_2	40.9	54.2	4.9	0.000	0.432	0.011	1.181	0.062	0.047	0.81	6.35
O_3	34.3	60.5	5.2	0.190	0.439	0.085	1.203	0.035	0.034	0.88	2.82

[a] Water retention curve (WRC) parameters according to the Van Genuchten model.
[b] Discrete compactness.
[c] Tortuosity.

Please cite this article as: Dal Ferro, N., et al., Application of smoothed particle hydrodynamics (SPH) and pore morphologic model to predict saturated water conductivity from X-ray..., Geoderma (2015), http://dx.doi.org/10.1016/j.geoderma.2015.04.019

3. Results and discussion

3.1. Soil structure properties

Total porosity ranged between a minimum of 0.432 $m^3\ m^{-3}$ and a maximum of 0.532 $m^3\ m^{-3}$ in the control (O_2) and liquid manure treatment ($L + r_1$), respectively. By contrast microCT porosity excluded all the pores smaller than 40 μm (Table 1) due to resolution limits and showed a total porosity of 0.066 $m^3\ m^{-3}$ on average, varying from a minimum of 0.015 $m^3\ m^{-3}$ and a maximum of 0.170 $m^3\ m^{-3}$, both in $L + r$. Pore size distribution (PSD), estimated from water retention curves according to the Young–Laplace capillary model, highlighted that soil porosity was mainly composed by pores < 40 μm as they represented 81.4% of total porosity, on average (Fig. 2a). Conversely microCT allowed only the analysis of pores > 40 μm (Fig. 2b), showing that the macropores were mostly distributed in the range of 40–1040 μm (86.0% on average) according to the PSD classification of Brewer (1964). An outlier was identified with microCT in the sample $L + r$ since a large pore, included during sampling, drastically increased both total porosity and pores larger than 1040 μm, biasing the representativeness of the core. MicroCT was able to detect such pore allowing for the visualization of the complex pore network larger than 40 μm while the WRC, that is based on the simple capillary bundle model (Hunt et al., 2013), probably overestimated the smaller pores due to the presence of "ink-bottle" necks.

X-ray analyses showed that microCT porosity within the soil samples was composed by a highly interconnected pore space (Table 1) that involved a high degree of connectivity between the voids (Dal Ferro et al., 2013), describing the main pore structure that spanned the soil cores (Fig. 1). For this reason K_{MORPHO} and K_{SPH} were calculated within such void network since it represented a pore continuity between the top and the bottom of each soil core. The discrete compactness (C_d) of the massive singular pore, establishing a relationship between the surface/volume ratio and the pore radius and contributing to hydraulic conductivity (Elliot et al., 2010), was always ≥0.81 (Table 1). While the massive singular pore did bridge the entire soil core, C_d indicated that the shape of the whole pore system was fairly spherical and could be described a single sphere (Bribiesca, 2008). Nevertheless, this parameter does not exclude concave regions or multiple-branch pores, although their structure might not be described by a capillary bundle model as also recently discussed by Hunt et al. (2013). Conversely, the pore system could have pore-pathways in all regions of the sample volume (Elliot et al., 2010). Finally, tortuosity of the pore space was 4.98 on average, which meant that the actual pore path was *ca.* five times larger than core height.

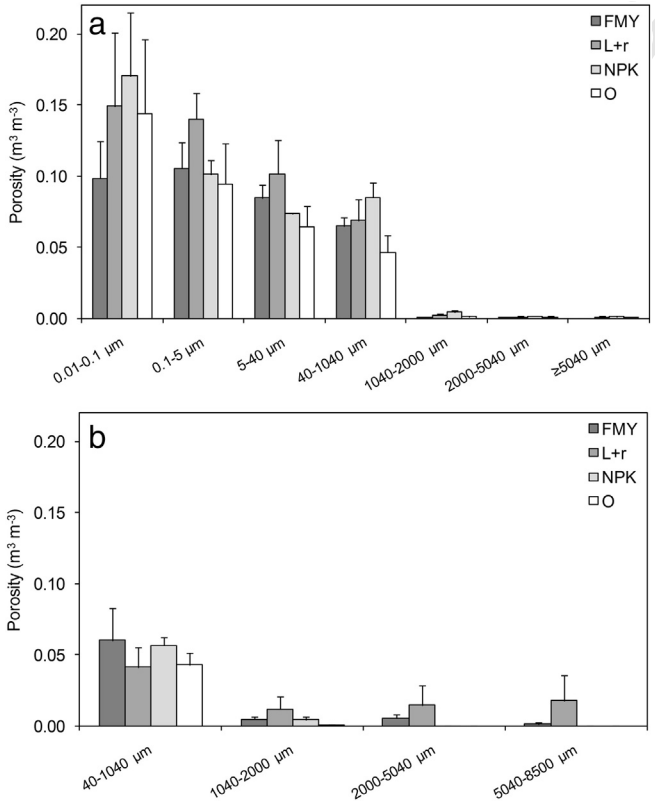

Fig. 2. Pore size distribution ($m^3\ m^{-3}$) estimated by means of (a) water retention curves and (b) X-ray microtomography. FMY = farmyard manure, L + r = liquid manure + residues, NPK = mineral fertilization and O = no fertilization control treatments.

3.2. Hydraulic conductivity

Experimental saturated hydraulic conductivity values (K_S) ranged from a minimum of $1.90 \cdot 10^{-6}$ m s^{-1} and a maximum of $4.27 \cdot 10^{-5}$ m s^{-1}, which is in line with previously reported values for the same soils (Morari, 2006). K_{SPH} data were similar to those experimentally measured at saturation, on average (geometric mean) $5.03 \cdot 10^{-6}$ m s^{-1} (Table 2) and varying between two orders of magnitude (10^{-5}–10^{-6} m s^{-1}), while lower values were found with the morphologic approach ($K_{MORPHO} = 1.26 \cdot 10^{-6}$ m s^{-1}). When modelled data were plotted vs. the experimental ones, a poor correlation was generally observed between the values. The correlation coefficient (R^2) varied between 0.098 and 0.790, with the best correlation found between K_{MORPHO} and K_{KC}. The poor correlation can be explained by the lack of diversity in the soil texture. Indeed the soil cores here analysed were characterized by similar texture properties (silty loam) as affected by the same pedogenic processes, making it difficult to distinguish between the subtle structure changes of each sample and, in turn, their influence on water flow. Moreover, a reduction of modelled water conductivity (Fig. 3) was noticeable when the soil structure was largely composed of thin pores that are often insufficiently imaged with microCT and thus underrepresented (e.g. in the control samples), especially in the vicinity of grain contacts (Andrä et al., 2013). By contrast, total porosity was a significant parameter for K_{MORPHO} estimations. This was highlighted by the strong correlation between K_{MORPHO} and total porosity (both from WRC and microCT, Table 3), and particularly emphasized when looking at Fig. 3b: in fact the O_1 and O_2 samples had both the lowest porosity and water conductivity; conversely $L + r_1$ was characterized by the highest porosity and K_{MORPHO}, suggesting the strong modelled water flow dependency on the total porosity.

Table 2
Comparison between the experimental hydraulic conductivity values (K_S) and those predicted using SPH (K_{SPH}) and the morphologic model (K_{MORPHO}) proposed by Elliot et al.(2010) and modified Kozeny–Carman equation (K_{KC}).

Soil Sample ID	Hydraulic conductivity (10^{-6} m s^{-1})			
	K_S	K_{SPH}	K_{MORPHO}	K_{KC}
FMY_1	6.31[a]	11.50	5.17	1.81
FMY_2	2.41[b]	10.50	4.13	2.07
FMY_3	7.41[a]	6.30	1.74	2.46
$L + r_1$	9.10[a]	10.00	40.29	4.53
$L + r_2$	42.74[a]	4.61	3.88	2.84
$L + r_3$	3.40[b]	1.20	0.28	1.00
NPK_1	17.50[a]	22.70	6.24	2.09
NPK_2	9.83[a]	2.78	0.35	1.87
NPK_3	27.03[a]	5.15	2.84	2.19
O_1	5.27[b]	2.40	0.04	0.31
O_2	2.22[b]	7.59	0.16	0.86
O_3	1.90[b]	1.04	0.25	1.39
Geometric mean	7.06	5.03	1.26	1.64

[a] Constant head method.
[b] Falling head method.

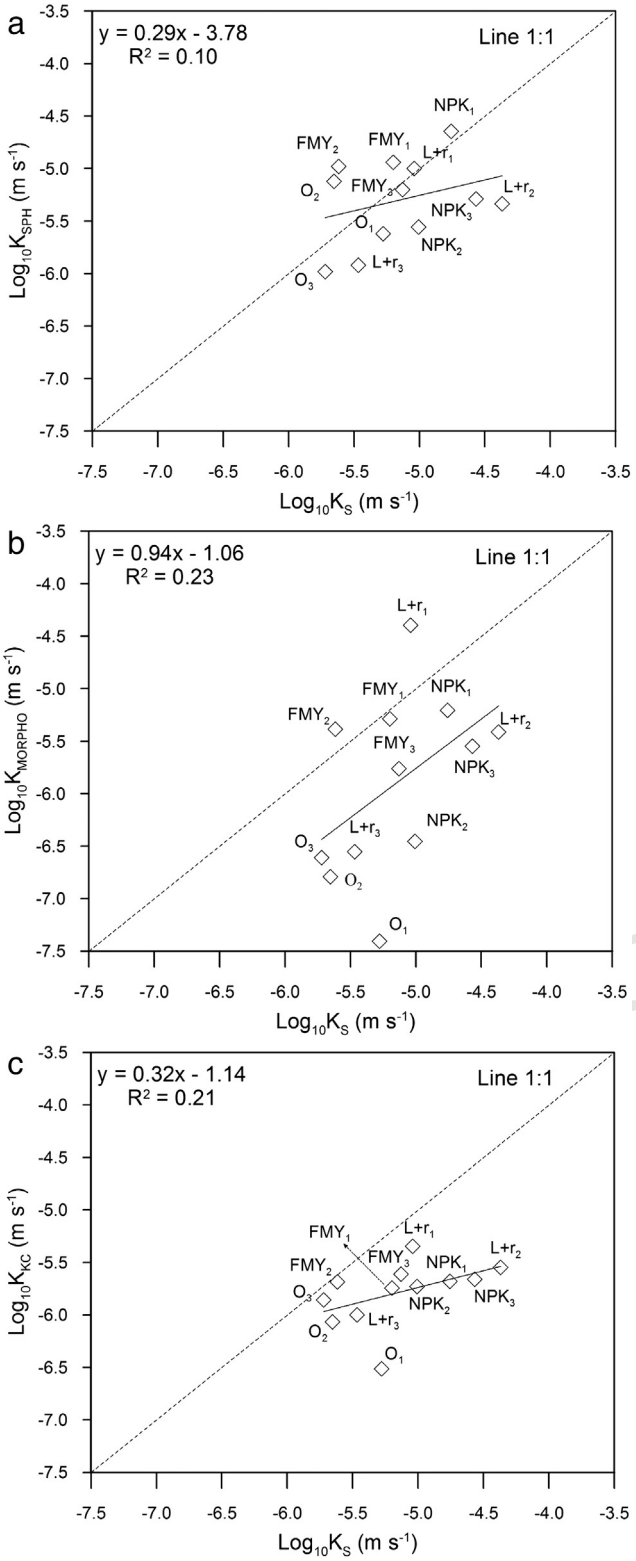

Fig. 3. Relationship between experimental (K_S) and predicted water conductivity according to values obtained using SPH (K_{SPH}), the morphological approach (K_{MORPHO}) proposed by Elliot et al. (2010) and semi-empirical Kozeny–Carman (K_{KC}).

Prediction of water velocity with SPH was higher than the experimental one in FMY_1 ($1.15 \cdot 10^{-5}$ m s^{-1} vs. $6.31 \cdot 10^{-6}$ m s^{-1}), FMY_2 ($1.05 \cdot 10^{-5}$ m s^{-1} vs. $2.41 \cdot 10^{-6}$ m s^{-1}), L + r_1 ($1.00 \cdot 10^{-5}$ m s^{-1} vs. $9.10 \cdot 10^{-6}$ m s^{-1}), NPK_1 ($2.27 \cdot 10^{-5}$ m s^{-1} vs. $1.75 \cdot 10^{-5}$ m s^{-1}) and O_2 ($7.59 \cdot 10^{-6}$ m s^{-1} vs.

Table 3
Correlation matrix between saturated hydraulic conductivity values and soil structure parameters determined by means of water retention curves (WRC) and microCT. P-values are reported in superscript numbers.

	WRC						MicroCT								
	Total porosity (m^3 m^{-3})	Pore size class (m^3 m^{-3})					Total porosity (m^3 m^{-3})	Largest pore (%)	Pore size class (m^3 m^{-3})				τ		C_d
		0.01–0.1	0.1–5	5–40	40–1040	1040–2000	2000–5040	≥5040			40–1040 μm	1040–2000 μm	2000–5040 μm	5040–8500 μm	
K_S	$0.83^{0.01}$	$0.26^{0.42}$	$-0.13^{0.68}$	$-0.03^{0.92}$	$0.72^{0.01}$	$0.65^{0.02}$	$0.46^{0.13}$	$0.81^{0.01}$	$0.10^{0.77}$	$0.03^{0.93}$	$0.02^{0.94}$	$0.24^{0.44}$	$0.09^{0.79}$	$0.050.87$	$0.22^{0.49}$	$0.03^{0.92}$
K_{SPH}	$0.34^{0.29}$	$-0.35^{0.26}$	$0.20^{0.54}$	$0.45^{0.15}$	$0.36^{0.24}$	$0.28^{0.37}$	$-0.14^{0.66}$	$0.14^{0.66}$	$0.62^{0.03}$	$0.42^{0.18}$	$0.64^{0.02}$	$0.49^{0.11}$	$0.32^{0.31}$	$0.250.43$	$0.34^{0.28}$	$-0.07^{0.82}$
K_{MORPHO}	$0.73^{0.01}$	$-0.48^{0.12}$	$0.29^{0.36}$	$0.66^{0.02}$	$0.62^{0.03}$	$0.27^{0.40}$	$-0.02^{0.96}$	$0.23^{0.47}$	$0.73^{0.01}$	$0.62^{0.03}$	$0.42^{0.18}$	$0.77^{0.00}$	$0.62^{0.03}$	$0.570.05$	$-0.22^{0.49}$	$0.48^{0.11}$
K_{KC}	$0.66^{0.02}$	$-0.45^{0.14}$	$0.26^{0.42}$	$0.58^{0.05}$	$0.71^{0.01}$	$0.29^{0.37}$	$0.20^{0.52}$	$0.27^{0.39}$	$0.59^{0.04}$	$0.65^{0.02}$	$0.32^{0.31}$	$0.61^{0.04}$	$0.53^{0.08}$	$0.470.12$	$-0.29^{0.35}$	$0.41^{0.19}$

$2.22 \cdot 10^{-6}$ m s^{-1}) (Table 2). By contrast, the lower K_{MORPHO} values than the experimental ones suggested the model inability to estimate water conductivity of soil-pore structures with a complex geometry. Similar results were also reported by Elliot et al. (2010), showing a general underestimation of modelled data with respect to the experimental ones as a result of potential preferential flow pathways which were not incorporated in the 3D image dataset. Positive correlations (Table 3) were observed between modelled water flow values and large-sized microCT PSD classes which emphasize the importance of conducting macropores (equivalent radius *ca.* > 400 μm) on water flow dynamics as reported in Jarvis (2007) and Beven and Germann (1982). However, no clear association was observed between more connected macropores and the increase of their size as was reported for some loamy and clayey soils (Larsbo et al., 2014), thus questioning the role of soil macropores on water flow dynamics. Most likely, K_{SPH} and K_{MORPHO} were also affected by the image resolution since water flow was estimated only for pores > 40 μm. Some authors (Peng et al., 2014) have reported a minor contribution of small pores on water permeability at a resolution < 12 μm, although in our case the invisible pores < 40 μm would have partially increased the water flow as they might act in two ways: a) the fluid flow is affected by the pore size channels and the prevalence of pores beyond the limits of microCT resolution (Fig. 2a) masked their effect on the fluid flow (Elliot et al., 2010); b) the massive singular pore through the entire soil core may have been even larger with a higher resolution of scanning, expanding the principal connected pore space and thus enhancing its representativeness of the sample (Blunt et al., 2013). For instance, the unconnected pores through the soil core NPK and represented in Fig. 1 (called "NPK sweep", orange and green pores) would have benefited of a higher scanning resolution ensuring their connection and improving water flow prediction to reach the experimental one. Moreover, K_{SPH} was affected by the pore connections as the water flow tended to zero where the pores were blind and water could not pass through them (Fig. 4, pores coloured in blue), reducing the overall hydraulic conductivity. Finally, according to the Stokes' law pore size affected the viscous forces which in turn grew from the centre of the pores (high velocity, pores coloured in red) to the solid surfaces of the soil matrix (pores coloured in blue) and reduced the SPH water velocity (Fig. 4).

Finally, experimental K_S and modelled results from microCT analysis were compared with data (K_{KC}) as determined by the Kozeny–Carman equation (Table 2), showing a consistent underestimation of K_{KC} with respect to K_S (Fig. 3c). The failure of the Kozeny–Carman could be partly affected by the spatial complexity of the porous medium since only simplified structural information is needed for its determination, excluding geometric and topologic data (Chen et al., 2008; Valdes-Parada et al., 2009).

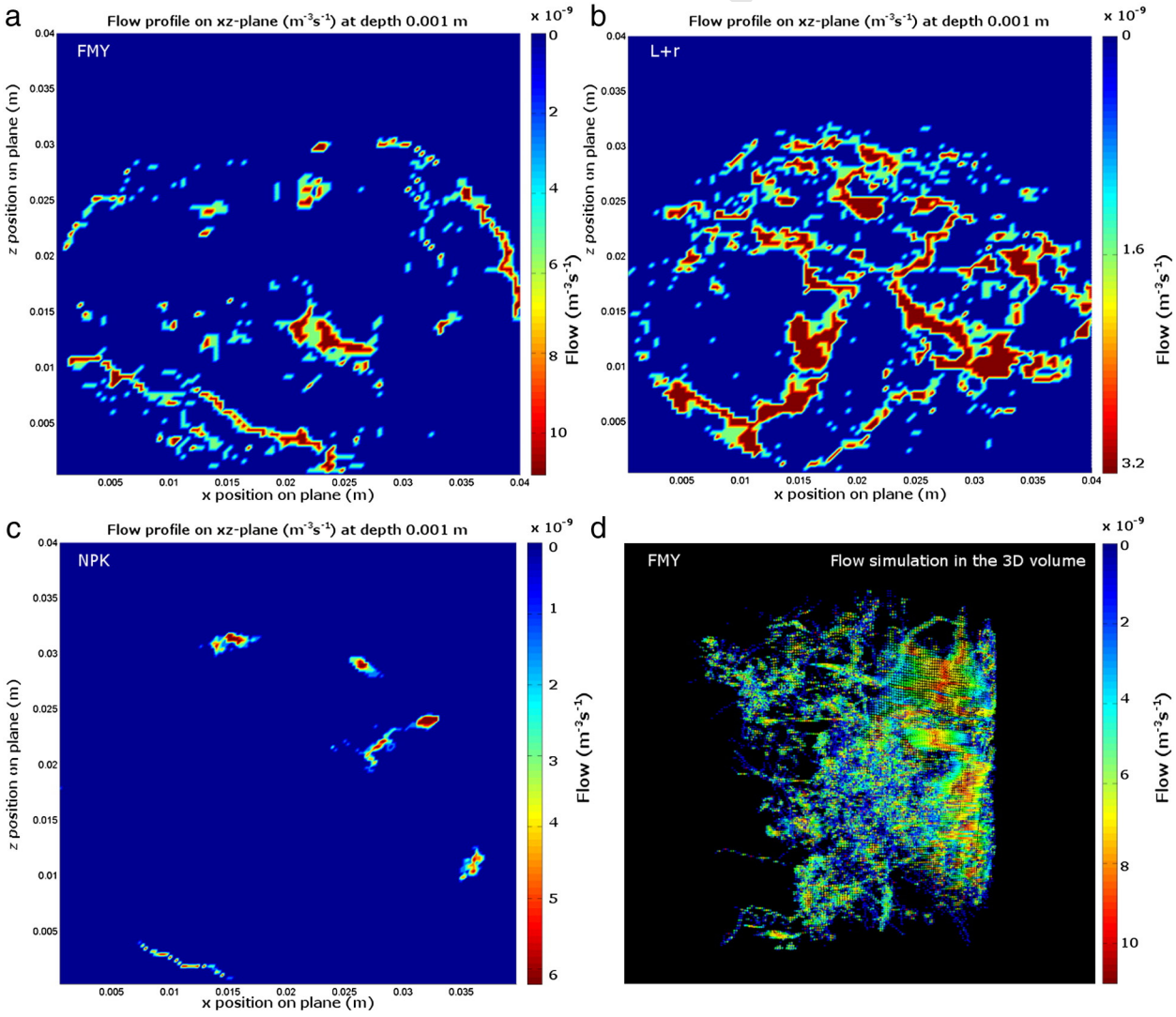

Fig. 4. Flow profile on xz-plane (m^3 s^{-1}) for soils characterized by (a) farmyard manure, (b) liquid manure + residues, (c) mineral fertilization treatments and on a 3D representation of the highly interconnected pore space (d, farmyard manure) using SPH.

Please cite this article as: Dal Ferro, N., et al., Application of smoothed particle hydrodynamics (SPH) and pore morphologic model to predict saturated water conductivity from X-ray..., Geoderma (2015), http://dx.doi.org/10.1016/j.geoderma.2015.04.019

4. Conclusions

Non-invasive acquisition of 3D soil information demonstrated its potential for the study of fluid flow through the pore network. The proposed SPH mesh-free method was able to simulate the water dynamics on large-sized complex samples with a good estimate of hydraulic conductivity values within the same order of magnitude of the experimental ones. The similarities between K_{SPH} and experimental data confirmed the major role of large conductive pores on the fluid flow, although a higher scanning resolution would have probably improved the water flow prediction. This was supported by the fact that microCT analysis was limited to pores larger than 40 μm, excluding the small connections from modelled conduction phenomena. A major role on K_{MORPHO} estimate was given by total porosity and pore size distribution, while the pore morphologic features played only a marginal role to influence water conductivity both for K_{SPH} and K_{MORPHO}. We hypothesized that pore morphology, although being able to affect the water flow through porous media, had here a secondary role in the definition of water conduction phenomena due to the presence of unique large macropore and a lack of variability in soils with similar texture properties. Expanding the present method to other soil types as well as increasing the spatial resolution are fundamental requirements to better understand the role of microporosity and the extent of representativeness of a massive singular pore on water conductivity.

References

Andrä, H., Combaret, N., Dvorkin, J., Glatt, E., Han, J., Kabel, M., Keehm, Y., Krzikalla, F., Lee, M., Madonna, C., 2013. Digital rock physics benchmarks—part II: computing effective properties. Comput. Geosci. 50, 33–43.

Arya, L.M., Heitman, J.L., Thapa, B.B., Bowman, D.C., 2010. Predicting saturated hydraulic conductivity of golf course sands from particle-size distribution. Soil Sci. Soc. Am. J. 74, 33–37.

Bear, J., 1972. Dynamics of Fluids in Porous Media. Elsevier, NY.

Bear, J., Bachmat, Y., 1990. Introduction to Modeling of Transport Phenomena in Porous Media. Kluwer, Dordrecht.

Beven, K., Germann, P., 1982. Macropores and water flow in soils. Water Resour. Res. 18, 1311–1325.

Blunt, M.J., Bijeljic, B., Dong, H., Gharbi, O., Iglauer, S., Mostaghimi, P., Paluszny, A., Pentland, C., 2013. Pore-scale imaging and modelling. Adv. Water Resour. 51, 197–216.

Bouma, J., 1989. Using soil survey data for quantitative land evaluation. Adv. Soil Sci. 9, 177–213.

Brewer, R., 1964. Fabric and Mineral Analysis of Soils. John Wiley, New York.

Bribiesca, E., 2000. A measure of compactness for 3D shapes. Comput. Math. Appl. 40, 1275–1284.

Bribiesca, E., 2008. An easy measure of compactness for 2D and 3D shapes. Pattern Recogn. 41, 543–554.

Bribiesca, E., Jimenez, J.R., Medina, V., Valdes, R., Yanez, O., 2003. A voxel-based measure of discrete compactness for brain imaging. Proceedings of the 25th Annual International Conference of the IEEE EMBS, Cancun, Mexico, pp. 910–913.

Chapuis, R.P., 2012. Predicting the saturated hydraulic conductivity of soils: a review. Bull. Eng. Geol. Environ. 71, 401–434.

Chen, C., Packman, A.I., Gaillard, J.F., 2008. Pore-scale analysis of permeability reduction resulting from colloid deposition. Geophys. Res. Lett. 35, 1–5.

Dal Ferro, N., Charrier, P., Morari, F., 2013. Dual-scale micro-CT assessment of soil structure in a long-term fertilization experiment. Geoderma 204, 84–93.

Doube, M., Kłosowski, M.M., Arganda-Carreras, I., Cordelières, F.P., Dougherty, R.P., Jackson, J.S., Schmid, B., Hutchinson, J.R., Shefelbine, S.J., 2010. BoneJ: free and extensible bone image analysis in ImageJ. Bone 47, 1076–1079.

Elliot, T.R., Reynolds, W.D., Heck, R.J., 2010. Use of existing pore models and X-ray computed tomography to predict saturated soil hydraulic conductivity. Geoderma 156, 133–142.

FAO-UNESCO, 1990. Soil Map of the World. Revised Legend. FAO, Rome.

Hunt, A.G., Ewing, R.P., Horton, R., 2013. What's wrong with soil physics? Soil Sci. Soc. Am. J. 77, 1877–1887.

Jarvis, N.J., 2007. A review of non-equilibrium water flow and solute transport in soil macropores: principles, controlling factors and consequences for water quality. Eur. J. Soil Sci. 58, 523–546.

Kozeny, J., 1953. Hydraulik: Ihre Grundlagen und praktische anwendung. Springer, Vienna.

Larsbo, M., Koestel, J., Jarvis, N., 2014. Relations between macropore network characteristics and the degree of preferential solute transport. Hydrol. Earth Syst. Sci. 18, 5255–5269.

Lee, T.C., Kashyap, R.L., Chu, C.N., 1994. Building skeleton models via 3-D medial surface/axis thinning algorithms. CVGIP: Graph. Model Image Process. 56, 462–478.

Leij, F.J., Alves, W.J., Van Genuchten, M.T., Williams, J.R., 1996. Unsaturated soil hydraulic database, UNSODA 1.0 user's manual. Rep. EPA/600/R96/095. USEPA, Ada, OK.

Lilly, A., 1996. A description of the HYPRES database (Hydraulic Properties of European Soils). In: Bruand, A., Duval, O., Wosten, J.H.M., Lilly, A. (Eds.), The Use of Pedotransfer Functions in Soil Hydrology Research. Proc. Workshop of the Project Using Existing Soil Data to Derive Hydraulic Parameters for Simulation Modelling in Environmental Studies and in Land Use Planning. Orleans, France, pp. 161–184.

Liu, G.R., Liu, M.B., 2003. Smoothed Particle Hydrodynamics: A Meshfree Particle Method. World Scientific Publishing Co., Singapore.

Liu, M.B., Liu, G.R., 2010. Smoothed particle hydrodynamics (SPH): an overview and recent developments. Arch. Comput. Methods Eng. 17, 25–76.

Luo, L., Lin, H., Li, S., 2010. Quantification of 3-D soil macropore networks in different soil types and land uses using computed tomography. J. Hydrol. 393, 53–64.

Maidment, D.R., 1993. Handbook of Hydrology. McGraw-Hill Inc., NY.

Monaghan, J.J., 1992. Smoothed particle hydrodynamics. Annu. Rev. Astron. Astrophys. 30, 543–574.

Morari, F., 2006. Drainage flux measurement and errors associated with automatic tension-controlled suction plates. Soil Sci. Soc. Am. J. 70, 1860–1871.

Morari, F., Lugato, E., Berti, A., Giardini, L., 2006. Long-term effects of recommended management practices on soil carbon changes and sequestration in north-eastern Italy. Soil Use Manage. 22, 71–81.

Narsilio, G.A., Buzzi, O., Fityus, S., Yun, T.S., Smith, D.W., 2009. Upscaling of Navier–Stokes equations in porous media: theoretical, numerical and experimental approach. Comput. Geotech. 36, 1200–1206.

Ovaysi, S., Piri, M., 2010. Direct pore-level modeling of incompressible fluid flow in porous media. J. Comput. Phys. 229, 7456–7476.

Pachepsky, Y.A., Rawls, W.J., Lin, H.S., 2006. Hydropedology and pedotransfer functions. Geoderma 131, 308–316.

Peng, S., Marone, F., Dultz, S., 2014. Resolution effect in X-ray microcomputed tomography imaging and small pore's contribution to permeability for a Berea sandstone. J. Hydrol. 510, 403–411.

Rawls, W.J., Gimenez, D., Grossman, R., 1998. Use of soil texture, bulk density, and slope of the water retention curve to predict saturated hydraulic conductivity. Trans. ASAE 41, 983–988.

Remy, E., Thiel, E., 2002. Medial axis for chamfer distances: computing look-up tables and neighbourhoods in 2D or 3D. Pattern Recogn. Lett. 23, 649–661.

Reynolds, W.D., Elrick, D.E., Youngs, E.G., Amoozegar, A., Booltink, H.W.G., Bouma, J., 2002. 3.4 Saturated and field-saturated water flow parameters. Methods of Soil Analysis Part 4 — Physical Methods. Dane J.H.; Topp, G.C., Madison, WI, pp. 797–801.

Serra, J., 1982. Image Analysis and Mathematical Morphology. Academic Press, London.

Strozzi, A.G., Duwig, C., Marquez, J., Prado, B., Delmas, P., Trujillo, F., Gamage, P., 2009. 3D porous media liquid–solid interaction simulation using SPH modeling and tomographic images. MVA2009 IAPR Conference on Machine Vision Applications, Yokohama, Japan, pp. 328–331.

Tartakovsky, A.M., Meakin, P., 2005. Simulation of unsaturated flow in complex fractures using smoothed particle hydrodynamics. Vadose Zone J. 4, 848–855.

Valdes-Parada, F.J., Ochoa-Tapia, J.A., Alvarez-Ramirez, J., 2009. Validity of the permeability Carman–Kozeny equation: a volume averaging approach. Physica A 388, 789–798.

Van Genuchten, M.T., Leij, F., Yates, S., 1991. The RETC code for quantifying the hydraulic functions of unsaturated soils. EPA/600/2-91/065. R.S. Kerr Environmental Research Laboratory, USEPA, Ada, OK.

Vereecken, H., Weynants, M., Javaux, M., Pachepsky, Y., Schaap, M.G., van Genuchten, M.T., 2010. Using pedotransfer functions to estimate the van Genuchten-Mualem soil hydraulic properties: a review. Vadose Zone J. 9, 795–820.

Wösten, J.H.M., Pachepsky, Y.A., Rawls, W.J., 2001. Pedotransfer functions: bridging the gap between available basic soil data and missing soil hydraulic characteristics. J. Hydrol. 251, 123–150.

Please cite this article as: Dal Ferro, N., et al., Application of smoothed particle hydrodynamics (SPH) and pore morphologic model to predict saturated water conductivity from X-ray..., Geoderma (2015), http://dx.doi.org/10.1016/j.geoderma.2015.04.019